AIP Journal of Applied Physics

Correlation between microstructure and temperature dependence of magnetic properties in Fe 60 Co 18 (Nb , Zr) 6 B 15 Cu 1 alloy series

J. S. Blázquez, V. Franco, C. F. Conde, A. Conde, J. Ferenc, T. Kulik, and L. F. Kiss

Citation: Journal of Applied Physics **105**, 093928 (2009); doi: 10.1063/1.3125515
View online: http://dx.doi.org/10.1063/1.3125515
View Table of Contents: http://scitation.aip.org/content/aip/journal/jap/105/9?ver=pdfcov
Published by the AIP Publishing

Correlation between microstructure and temperature dependence of magnetic properties in $Fe_{60}Co_{18}(Nb,Zr)_6B_{15}Cu_1$ alloy series

J. S. Blázquez,[1] V. Franco,[1] C. F. Conde,[1] A. Conde,[1,a)] J. Ferenc,[2] T. Kulik,[2] and L. F. Kiss[3]
[1]*Departamento de Física de la Materia Condensada, ICMSE-CSIC, Universidad de Sevilla, P.O. Box 1065, 41080 Sevilla, Spain*
[2]*Faculty of Materials Science and Engineering, Warsaw University of Technology, ul. Woloska 141, 02-507 Warsaw, Poland*
[3]*Research Institute for Solid State Physics and Optics, Hungarian Academy of Science, P.O. Box 49, 1525 Budapest, Hungary*

(Received 9 January 2009; accepted 1 April 2009; published online 14 May 2009)

Temperature dependence of magnetic properties of nanocrystalline $Fe_{60}Co_{18}Cu_1B_{15}Nb_{6-x}Zr_x$ (x=0, 3, 6) alloys has been studied at different stages of devitrification. Transmission electron microscopy shows nanocrystals of the size ~5 nm, which remains almost constant along the nanocrystallization process. Curie temperature of the residual amorphous phase decreases as nanocrystallization progresses for all the studied alloys. Thermal dependence of the exchange stiffness constant is obtained from the measurement of specific magnetization and coercivity as a function of crystalline fraction and temperature for the three studied alloys. © *2009 American Institute of Physics*. [DOI: 10.1063/1.3125515]

I. INTRODUCTION

Soft magnetic Fe-based nanocrystalline alloys[1] are among the softest magnetic materials known. The interest of the scientific community on this field was attracted by the work of Yoshizawa *et al.*[2] in which the fabrication of Fe–Si–Nb–B–Cu (Finemet) alloys was reported. Besides this one, following works focused mainly on other families of alloys: Fe–(Nb,Zr,Hf,…)–B–(Cu) (Nanoperm) (Ref. 3) and Fe–Co–(Nb,Zr,Hf,…)–B–(Cu) (Hitperm).[4] In the case of Hitperm alloys, they were developed in the aim of extending the soft magnetic properties to higher temperatures as previous systems lost their magnetic softness at the relatively low Curie temperature of the residual amorphous phase. Consequently, high temperature behavior of Hitperm alloys has been studied in recent years from the application point of view.[5–10]

Cu addition is expected to form Cu rich clusters prior to the nanocrystallization process, leading to a refinement of the nanocrystalline microstructure. Strong differences were observed between Hitperm alloys containing Zr or Nb with higher Co content (Fe to Co content ratio, Fe/Co=0.5). Whereas Cu clusters are not formed in Hitperm alloys containing Zr,[11] they are clearly detected for Hitperm alloys containing Nb.[12] In fact, microstructure refinement is clearly observed after 1 at. % Cu addition in Hitperm alloys containing Nb with 18 at. % Co.[13] If no Cu is added to this alloy, nanocrystallization shows the formation of very irregular nanocrystals (~25 nm in size) whose shape can be interpreted as agglomerates of smaller and more regular units (~5 nm in size). This microstructure is very similar to that found in Hitperm alloys containing Zr with Fe/Co=0.5, where Cu clustering phenomenon is absent.[11]

The peculiar microstructure exhibited by these alloys, in which ferromagnetic nanosized crystallites are embedded in a ferromagnetic residual amorphous phase with a lower Curie temperature, is responsible for their outstanding soft magnetic properties. Herzer[14] successfully explained the main features observed in the magnetic behavior of these nanocrystalline alloys. However, Herzer's model concerns a single nanocrystalline phase with an average crystal size $\langle D \rangle$, describing the coercivity dependence on crystal size by the well known $\langle D \rangle^6$ power law,[14] but nanocrystalline systems developed by controlled crystallization of an amorphous precursor alloy always consist at least of two phases: nanocrystals plus residual amorphous matrix. Thus, Herzer's original model fails to describe the thermal dependence of coercivity close to the Curie temperature of the amorphous phase and its rise observed at the very beginning of nanocrystallization. Some years after Herzer's work, Hernando *et al.*[15] and Suzuki and Cadogan[16] extended Herzer's model to biphasic systems.

In this work, thermal and microstructural dependences of magnetic properties are reported for a low Co containing Hitperm series with partial or total substitution of Zr for Nb. Studies on the effect of the early transition metal (Zr, Nb, Ta, Hf) on the crystallization, microstructure and magnetic properties can be found in literature for Hitperm alloys with medium[17] and high[18] Co content.

Results obtained in this study were quantitatively analyzed in the frame of the two phase model developed by Hernando *et al.*[15] and Suzuki and Cadogan.[16] Therefore, it will be helpful to recall some ideas concerning these models.[14–16,19]

The effective magnetic anisotropy, K_{exp}, of a system is proportional to the product of the saturation magnetization, M_S, and the coercivity, H_C:

a)Electronic mail: conde@us.es. Tel.: (34)-95-455-28-85. FAX: (34)-95-461-20-97.

$$p_C K_{\exp} = \mu_0 H_C M_S, \tag{1}$$

where p_C is a constant (~0.2 for Finemet alloys and 0.64 for cubic crystals[16]) and μ_0 is the magnetic permeability of vacuum.

On the other hand, the observed anisotropy is a combination of different contributions: mainly magnetocrystalline, K_C, and induced, K_U, anisotropies.

$$K_{\exp} = \sqrt{\langle K_C \rangle^2 + \langle K_U \rangle^2}. \tag{2}$$

In the previous expression, average values are used due to the complexity of the system. Finally, the crystalline contribution to the anisotropy would be affected by the crystalline fraction, X_C, and can be expressed as[16,19]

$$\langle K_C \rangle = X_C^2 \langle K_C^{\text{nano}} \rangle = X_C^2 \frac{K_1^4 \langle D \rangle^6}{A^3}, \tag{3}$$

where K_1 is the magnetocrystalline anisotropy constant of the crystalline phase (~10^4 J m^{-3}) (Ref. 20) and A is the exchange stiffness constant. The thermal and microstructural dependences of this parameter for the low Co containing Hitperm series studied in this work will be also reported.

II. EXPERIMENTAL

Amorphous ribbons (~5 mm wide and 20–30 μm thick) with nominal compositions $Fe_{60}Co_{18}Cu_1B_{15}Nb_{6-x}Zr_x$ (x=0, 3, 6) (in the following referred to as Nb, NbZr and Zr alloys, respectively) were prepared by melt-spinning technique. Previous differential scanning calorimetry (DSC) experiments[21] showed that the devitrification of these alloys occurs in several transformation steps, evidenced by exothermic processes. In the first one, α-Fe,Co nanocrystals appear embedded in a residual amorphous matrix enriched in B and Nb and/or Zr. In order to study the nanocrystallization process and its effect on the magnetic properties, several nanocrystalline samples were prepared by heating amorphous as-cast ribbon pieces (6 mm long) at 20 K/min up to selected temperatures in vacuum in a halogen lamp furnace. The final temperatures were chosen in order to achieve 10%, 30%, 60%, and 90% of the enthalpy ascribed to the nanocrystallization process. This fraction will be named in the following as nanocrystallization fraction and denoted by X_{DSC}.

Microstructure was studied at room temperature by transmission electron microscopy (TEM) (Philips CM200 operated at 200 kV) and Mössbauer spectroscopy, (MS) in a transmission geometry using a ^{57}Co(Rh) source. The incident γ-beam was perpendicular to the ribbon plane. Values of the hyperfine parameters were obtained by fitting with NORMOS program.[22] The isomer shift (IS), was quoted relative to the Mössbauer spectrum of an α-Fe foil at room temperature.

Thermomagnetic gravimetry (TMG) (Perkin-Elmer TGA-7) experiments were performed applying the magnetic field of a small magnet (~20 mT). Changes in the magnetic force acting upon the sample are related to the variations in magnetization with temperature, and recorded as apparent weight changes in the sample. Permeability measurements were performed on toroidal samples at a frequency of 6 kHz and an applied field small enough (~1 A/m) to assure the measurement of the initial permeability, μ. The experiment consisted of several heating-cooling cycles and both measurement and heat treatment of the samples were performed at the same time. For these measurements, two coils were wound around the toroidal sample. An ac field was applied to the sample using the first coil, whereas the signal induced in the second coil was detected using a lock-in technique. An impedance analyzer (Hewlett-Packard 4192A) was used to calibrate the values of μ at room temperature. High temperature hysteresis loops were recorded using a quasistatic hysteresis loop tracer. The loops were measured in a continuous heating mode but with so slow a heating rate that, during the acquisition time (~30 s), the temperature at the sample rose less than 3 K. The absence of microstructural evolution during the measurements was checked by comparing the coercivity of each sample at room temperature before and after measuring at high temperatures. Saturation magnetization was measured at different temperatures by vibrating sample magnetometry (VSM) (Lakeshore 7407).

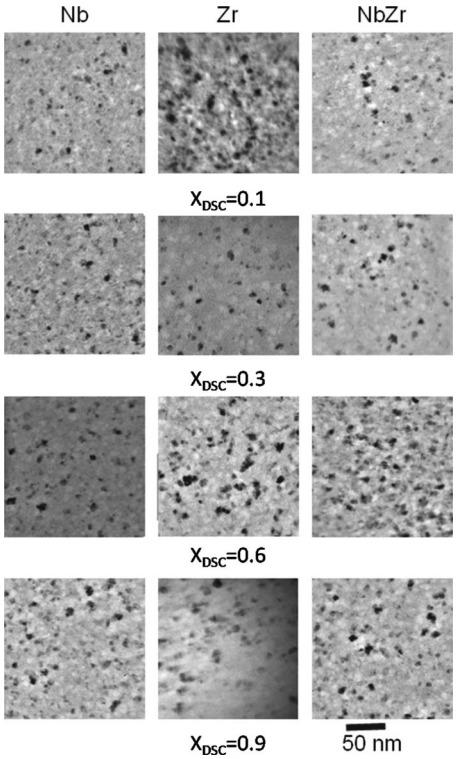

FIG. 1. Bright field TEM images of the different studied samples.

III. RESULTS

A. Transmission electron microscopy

Figure 1 shows bright field TEM images of the different studied samples. Nanocrystalline microstructure is clearly observed in all cases and selected area diffraction patterns confirm the bcc structure of the nanocrystals, in agreement with previous x-ray diffraction studies.[21] Figure 2 shows histograms for crystal size distribution of each studied sample. There is a slight increase in the average crystal size, $\langle D \rangle$, as nanocrystallization progresses: from X_{DSC}=0.1 to 0.9, $\langle D \rangle$

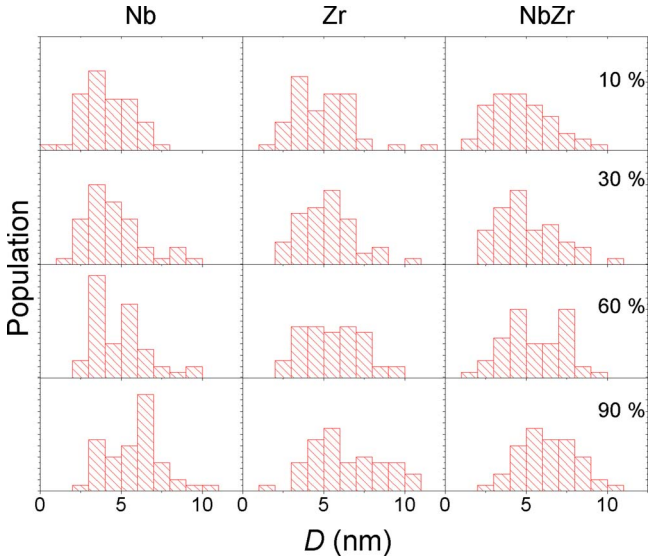

FIG. 2. (Color online) Crystal size distribution histograms of the different studied samples. Percentages pertain to percent crystallized.

changes from 4.2 to 5.7 nm for Nb alloy, from 4.9 to 6.4 nm for Zr alloy and from 4.7 to 6.2 nm for NbZr alloy, with $\Delta\langle D\rangle = \sigma/\sqrt{N} = \pm 0.3$, where σ is the standard deviation of the corresponding crystal size distribution of Fig. 2 and $N = 50$, the number of the measured crystals. These small changes are in agreement with the instantaneous growth approximation describing the nanocrystallization kinetics of this kind of alloy.[23,24] Under this approach, the time required for a nanocrystal to achieve its final size is negligible in comparison with the time of nanocrystallization process.

In the present study, no differences appear after partial or total substitution of Zr for Nb. In all the studied samples, the shape of the crystals was regular (no agglomerates were appreciated) and their average size clearly lower than that of $Fe_{44}Co_{44}Zr_7B_4Cu_1$ alloy.[11] These facts indicate that Cu cluster must form in the studied alloy series (having a lower Co content than the alloy studied in Ref. 11), independently of the amount of Zr, to achieve the observed refinement. It is worth mentioning that the amount of B in the studied alloy is higher than that of Hitperm alloys containing Zr, where no Cu clustering phenomenon is reported.

B. Mössbauer spectrometry

Figure 3 shows, as an example, Mössbauer spectra of as-cast and nanocrystallized samples for NbZr alloy. For all the studied alloys, as-cast samples exhibit a typical very broad sextet characteristic of amorphous ferromagnets but, as nanocrystallization progresses, a new and sharper sextet grows at higher values of velocity, ascribed to α-Fe,Co nanocrystals. Although the spectra of amorphous samples could be fitted using a single distribution of magnetic hyperfine fields (HFs), nanocrystallized samples need a more complex model. In the studied case, four discrete sextets and two different HF distributions were used. The discrete sextets (pure crystalline contributions) are necessary to represent the different Fe environment (characterized by the number of Co neighbors) existing in a bcc phase with an expected composition $Fe_{82}Co_{18}$.[12] The two HF distributions can be roughly ascribed to Fe atoms in the amorphous phase (low field contribution) and to Fe atoms at interface regions (high field contribution with HF < 33 T). The aim of using two different HF distributions is to preserve the different nature of both contributions: Fe located in amorphous regions and Fe located at interface regions. Pure crystalline contribution and the sum of both HF distributions for NbZr alloy are also represented in Fig. 3 along with the experimental data and the total fitting. The probability distribution for the different hyperfine field contributions obtained from the fitting is also shown as an example for NbZr alloy in this figure.

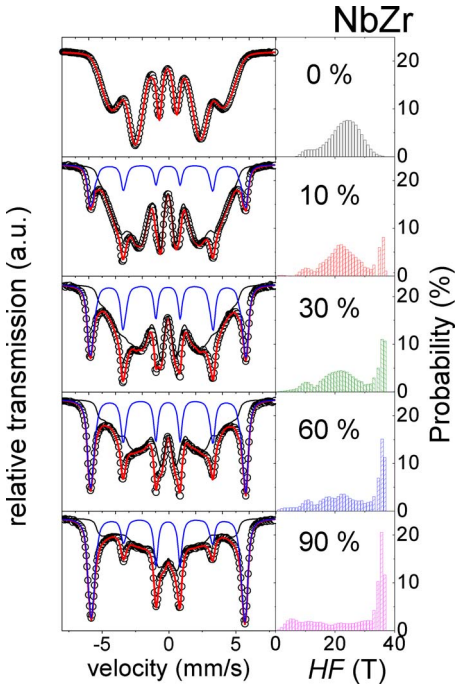

FIG. 3. (Color online) Mössbauer spectra and hyperfine field distribution of $Fe_{60}Co_{18}Nb_3Zr_3B_{15}Cu_1$ amorphous and nanocrystalline samples. Percentages pertain to percent crystallized.

The average values derived from the fitting procedure (magnetic hyperfine field, $\langle HF\rangle$; isomer shift, $\langle IS\rangle$; intensity ratio between the second and third lines of the sextets, $\langle R_{23}\rangle$) and the area fraction of pure crystalline contributions, A_{cryst}, are shown in Fig. 4 as a function of X_{DSC}. The continuous increase of A_{cryst} with X_{DSC} is due to the close relationship between these two parameters. However, they are sensitive to different features of the crystallization process and some information can be extracted from a deeper comparison. X_{DSC} is the enthalpy needed to achieve a certain nanocrystalline microstructure normalized to the enthalpy released after completing the nanocrystallization process. A_{cryst} is the fraction of Fe atoms in pure crystalline sites (without taking into account Fe atoms at interface). As a first approximation, both magnitudes can be considered proportional to the crystalline volume fraction. Moreover, a constant composition of the formed α-Fe,Co phase along the nanocrystallization process supports this approximation. Although this approximation is well described for nanocrystalline samples by a linear dependence between both magnitudes, this linearity cannot be extended to $X_{DSC}=0$ (see Fig. 4). In fact, the evolution of

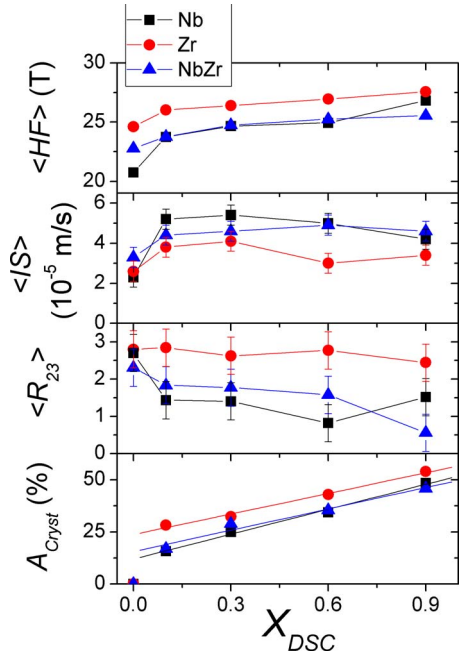

FIG. 4. (Color online) Average hyperfine magnetic field, ⟨HF⟩, average isomer shift, ⟨IS⟩, relative intensity between the second and third lines, R_{23}, and area corresponding to the discrete sextets used in the fitting procedure, A_{cryst}, as a function of the crystallization fraction. Lines are a guide to the eye except for A_{cryst} plot, where they represent linear fittings to the data.

A_{cryst} for $X_{DSC}<0.1$ is faster than for $X_{DSC}>0.1$ for the three studied alloys, i.e., the enthalpy per Fe atom incorporated to pure crystalline sites is smaller at the very early stages of nanocrystallization than after $X_{DSC}>0.1$. This can be understood in the frame of a recently proposed crystallization mechanism for these nanocrystalline systems based on continuous nucleation and instantaneous growth processes.[23,24] This mechanism predicts faster crystallization kinetics (although slow in comparison with conventional nucleation and three dimensional growth mechanisms) at the very beginning of nanocrystallization process, characterized by an Avrami exponent close to 1, which decreases as nanocrystallization progresses. The slowing down of the kinetics after the early stages of nanocrystallization can be correlated with a larger enthalpy per Fe atom incorporated to crystalline sites, i.e., with a more difficult mechanism of crystallization. This is expected in the continuous nucleation and instantaneous growth approach as the available volume to form new nuclei reduces as the process progresses. Interface contribution, A_{int}, must be considered also as a crystalline contribution in order to appropriately calculate the crystalline volume fraction, X_C,[25] being $X_C \propto (A_{cryst}+A_{int})$. However, as crystalline size does not change significantly (supporting instantaneous growth approximation for this kind of alloys), interface contribution will be almost constant not affecting the linearity exhibited by the A_{cryst} versus X_{DSC} plot in Fig. 4.

The parameter $\langle R_{23}\rangle$ can be linked with the average angle between the hyperfine magnetic field and the incident γ beam, θ, from

$$\langle R_{23}\rangle = \frac{4\sin^2\theta}{1+\cos^2\theta}. \quad (4)$$

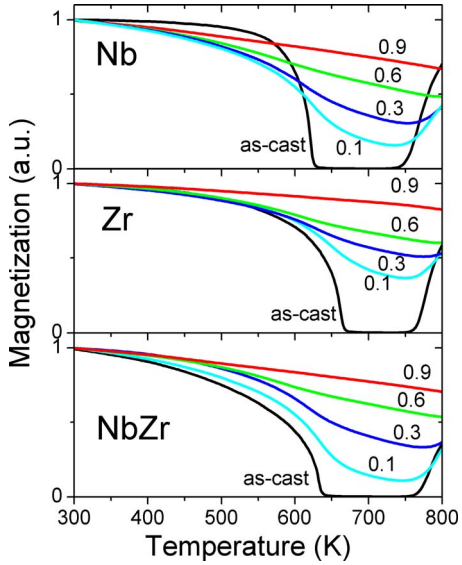

FIG. 5. (Color online) TMG plots of the different studied samples.

For Nb and NbZr alloys, the angle decreases as nanocrystallization progresses, for Zr alloy it remains almost constant independent of X_{DSC}.

C. Thermomagnetic gravimetry

Figure 5 shows TMG plots for as-cast and nanocrystalline samples of the three studied alloys. For as-cast samples, a first fall to zero between 600 and 700 K is observed for all the studied alloys due to the Curie transition temperature of the amorphous phase. About 750 K, a rise in the relative magnetization indicates the onset of nanocrystallization, in agreement with DSC results.[21] As nanocrystallization progresses, magnetization does not fall to zero because of the formed ferromagnetic α-Fe,Co phase which has a higher Curie temperature than the amorphous one and higher than the explored range. The rise in magnetization shifts to higher temperatures in agreement with the enhancement of thermal stability during nanocrystallization.

D. Thermal dependence of the initial permeability

Figure 6 shows initial permeability, μ, versus temperature. These *in situ* measurements were performed starting from an amorphous as-cast sample and both thermal treatment and measurement were done at the same time during several heating-cooling cycles, progressively increasing the maximum temperature of the nth cycle, $T_{heat}(n)$. After comparing the cooling branch of the nth cycle with the heating one corresponding to the $(n+1)$th cycle, it can be observed that μ is reversible up to $\sim T_{heat}(n)$ of the nth cycle. Heating to temperatures below crystallization onset yields an increase of μ due to strain relaxation and, for these amorphous samples, a clear Hopkinson peak is observed at the Curie temperature of the amorphous phase. Heating above nanocrystallization onset leads to an irreversible rise of μ ascribed to formation of α-Fe,Co phase. After cooling down nanocrystallized samples, for low crystalline volume fractions, μ at room temperature increases with respect to that of amorphous samples and reaches a maximum. Moreover, the Hop-

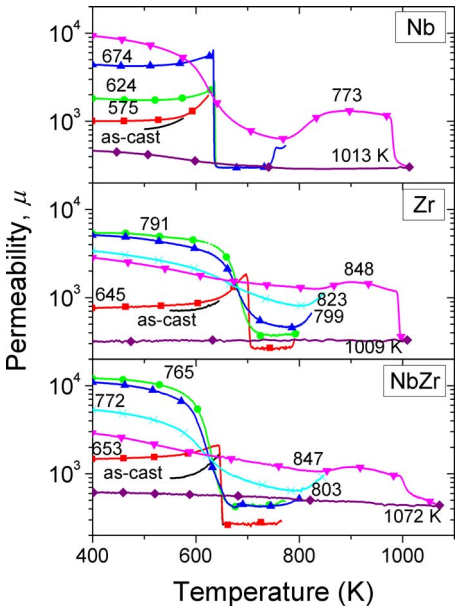

FIG. 6. (Color online) Initial permeability measurements of the three studied alloys during several heating-cooling cycles. Curves are identified by the corresponding maximum temperature achieved during the previous heating.

kinson peak is no longer observed but the fall of μ is continuous and smoother as T_{heat} increases. As nanocrystallization progresses, the value of μ at room temperature decreases with respect to the maximum value achieved at very low crystalline fractions when the softest sample is obtained at room temperature. However, the value of μ at high temperature increases, leading to a smaller coefficient of the dependence of μ with temperature. Heating above the second transformation stage observed by DSC,[21] an irreversible fall in μ is observed, ascribed to the formation of boride phases, which magnetically harden the material.

E. Thermal dependence of coercivity

Figure 7 shows the temperature dependence of coercive field, H_C, for nanocrystalline samples as a function of the

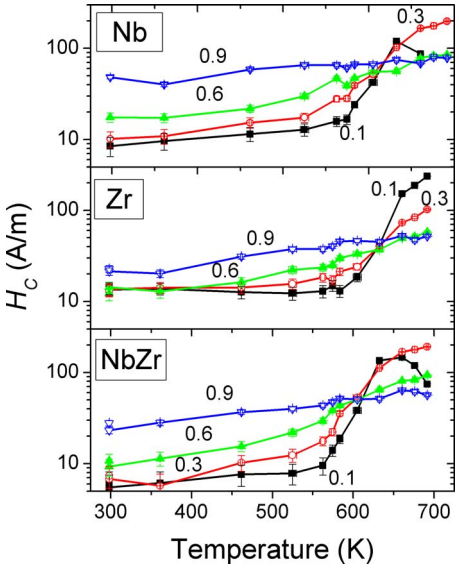

FIG. 7. (Color online) Coercivity of the different studied samples as a function of temperature. Lines are a guide to the eye.

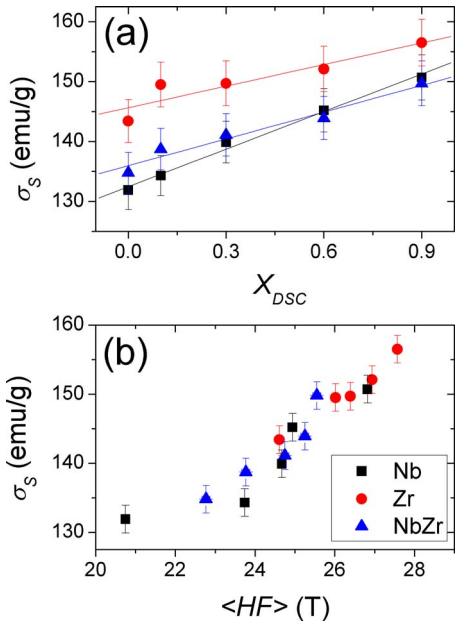

FIG. 8. (Color online) Specific magnetization as a function of (a) crystallization fraction (lines correspond to linear fitting of the data) and (b) average hyperfine magnetic field.

degree of nanocrystallization. In agreement with initial permeability results, the softest sample is obtained for very low crystalline fraction, independent of the studied alloy. For these samples, X_{DSC}=0.1, a clear increase in H_C is observed at elevated temperatures due to the ferroparamagnetic transition of the amorphous phase. As this phase becomes paramagnetic, the exchange coupling between nanocrystals is lost and only dipolar interactions prevent the system from becoming a set of isolated superparamagnetic particles.[26] The anhysteretic superparamagnetic state is expected to be achieved at higher temperatures than those explored here. As nanocrystallization progresses, the observed relative increase in H_C, defined as $R_{H_C}=[H_C(T_{max})-H_C(300\ \mathrm{K})]/H_C(300\ \mathrm{K})$, where T_{max} is the temperature at which the maximum value of H_C is achieved, drastically drops from X_{DSC}=0.1 to 0.9 (from $R_{HC}\sim 1800\%$ to 150% and 170% for the Zr and NbZr alloys, respectively, and from $R_{HC}\sim 1100\%$ to 65% for Nb alloy).

F. Saturation magnetization

Saturation magnetization values were obtained from magnetization curves, $M(H)$, using a VSM with a maximum applied field of 1.5 T. The linear behavior of $M(H)$ at high field ($H>0.5$ T) was extrapolated to H=0 and the saturation magnetization was measured as the intersection of this line with H=0. Figure 8(a) shows the values obtained at room temperature for the different alloys as a function of the nanocrystallization fraction. Figure 8(b) shows the relationship (close to linear) existing between specific magnetization, σ_S, and $\langle HF\rangle$, also observed for other amorphous and nanocrystalline systems.[25]

A linear increase is observed in Fig. 8(a) as nanocrystallization progresses, which can be understood from a very simple two phase model described by the following expression:

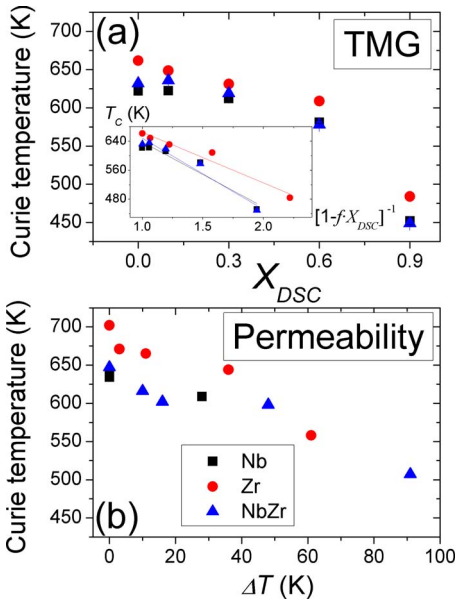

FIG. 9. (Color online) Curie temperature as a function of the progress of nanocrystallization: (a) from TMG plots vs crystallization fraction and (b) from permeability measurements vs the thermal span from the crystallization onset temperature and the maximum temperature achieved during treatment. The inset of (a) corresponds to the data as a function of the enrichment in Nb/Zr and B in the amorphous matrix. Lines correspond to linear fitting of the data.

$$\sigma_S = X_C \sigma_s^{\text{cryst}} + (1 - X_C)\sigma_s^{\text{amorph}}, \tag{5}$$

where X_C is the crystalline volume fraction, $X_C = fX_{\text{DSC}}$ (f being the maximum crystalline fraction achieved, $f=0.54$ for this alloy[27]) and σ_S^{cryst} and σ_S^{amorph} are the specific magnetization of the crystalline and amorphous phases, respectively. Therefore, a linear increase of the total specific magnetization, σ_S, with X_{DSC} is obtained with a slope $s = f(\sigma_S^{\text{cryst}} - \sigma_S^{\text{amorph}})$. Although the constant composition of the nanocrystals along the nanocrystallization process supports σ_S^{cryst} to be constant, this approach cannot be so easily assumed for σ_S^{amorph}, as the composition of this phase continuously changes. Therefore, σ_S^{amorph} is rather considered as an average value. The results obtained from the linear fitting are $\sigma_S^{\text{amorph}} = 132.4 \pm 0.5$, 145.6 ± 1.4, and 136.0 ± 0.8 emu/g; and $\sigma_S^{\text{cryst}} = 171 \pm 3$, 168 ± 7, and 164 ± 4 emu/g for Nb, Zr, and NbZr alloys, respectively. In the case of σ_S^{cryst}, changes among the different studied alloys are within the error bar as the expected composition of the crystalline phase developed in the three studied alloys is the same. However, this value is smaller than that of pure crystalline Fe at room temperature, 218 emu/g,[28] ascribed to the nanocrystalline nature of the crystalline phase studied.

IV. DISCUSSION

A. Curie temperature of the amorphous phase

Curie temperature was measured from both TMG and permeability measurements. In each case, the derivative of the signal was calculated and the inflexion point was taken as indicative of the Curie temperature (Fig. 9). Both techniques agree describing a continuous decrease in the Curie temperature with the progress of the nanocrystallization process from the value corresponding to the fully amorphous system. Although this behavior has been reported for some nanocrystalline systems [e.g., $(FeCr)_{73.5}Si_{13.5}B_9Nb_3Cu_1$ (Ref. 29)], the opposite behavior is also reported for similar alloys [e.g., $Fe_{63}Co_{20}Ge_5Zr_6B_5Cu_1$,[10] $Fe_{90}Zr_7B_2Cu_1$,[30] $Fe_{91-x}Mo_8Cu_1B_x$ (Ref. 31)]. On the other hand, an initial rise in Curie temperature for samples heated up to the early stages of nanocrystallization followed by a continuous decrease of the Curie temperature of the amorphous phase as nanocrystallization progresses is also observed in some nanocrystalline systems [e.g., $Fe_{78}Co_5Ge_5Zr_6B_5Cu_1$,[10] $Fe_{68.5}Mo_5Si_{13.5}B_9Cu_1Nb_3$ (Ref. 32)]. In fact, this decrease is opposite to the expected increase due to the presence of nanocrystals with a high Curie temperature (α-Fe,Co), which should polarize the amorphous matrix. Compositional changes in the amorphous matrix, impoverishment in Fe and enrichment in Nb and/or Zr as the nanocrystallization progresses, seem to be more important effects and yield a reduction in the Curie temperature in the studied case.

This compositional effect could be clarified considering that the concentration of an element i in the amorphous matrix, C_i^{am}, and in the crystalline phase, C_i^{cr}, are linked with the average concentration in the alloy, C_i^{total}:

$$C_i^{\text{total}} = X_C C_i^{\text{cr}} + (1 - X_C) C_i^{\text{am}}, \tag{6}$$

where $X_C = fX_{\text{DSC}}$, as stated above. Therefore, the concentration of B and Zr/Nb in the amorphous matrix will increase as these elements have a very low solubility in the crystalline phase:

$$C_{(\text{Zr,Nb})+\text{B}}^{\text{Am}} = \frac{C_{(\text{Zr,Nb})+\text{B}}^{\text{total}}}{1 - fX_{\text{DSC}}}. \tag{7}$$

The inset of Fig. 9 shows an approximately linear decrease in Curie temperature with the progressive increase of B, Zr, and/or Nb in the amorphous matrix. Although an increase in B should lead to an increase in the Curie temperature, it seems that the effect of enrichment in Zr and/or Nb (Ref. 33) is predominant.

B. Thermal dependence of magnetic properties

The K_{exp} values of expression (1) can be calculated from the present experimental data after changing from σ_S (obtained in emu/g from VSM at the different studied temperatures) to $\mu_0 M_S$ (in T) taking into account the density of the material, which is approximately $\rho \sim 8 \times 10^3$ kg/m^3.

Combining previous expressions it is possible to find

$$(\mu_0 M_S H_C)^2 = p_C^2 \left(f^4 X_{\text{DSC}}^4 \frac{K_1^8 \langle D \rangle^{12}}{A^6} + \langle K_U \rangle^2 \right), \tag{8}$$

where M_S, H_C, and $\langle D \rangle$ have been measured in this work as a function of temperature, X_{DSC} and composition.

Nanocrystallization leads to a negligible change in the magnetostriction of the studied alloys,[34] unlike the reduction observed in Finemet alloys[2] or the strong increase observed for Hitperm alloys with higher Co content.[34] This fact allows us to consider $\langle K_U \rangle$ to be independent of X_{DSC} assuming stresses are independent of X_{DSC} for each composition. On the other hand, as established by TEM, changes in $\langle D \rangle$ are negligible and instantaneous growth can describe the kinetics

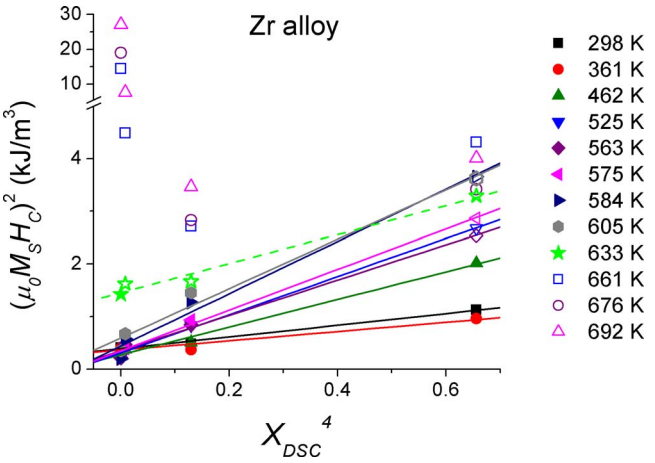

FIG. 10. (Color online) Square of the effective magnetic anisotropy vs the fourth power of the crystallization fraction for $Fe_{60}Co_{18}Zr_6B_{15}Cu_1$. Solid symbols correspond to those data obtained at a temperature below that of their corresponding amorphous Curie temperature. Hollow symbols identify those data obtained at temperatures above their corresponding amorphous Curie temperature. Solid lines correspond to linear fittings with $r>0.9$ (r is regression factor), the dashed line corresponds to the first set of data which deviated from the expected linearity. It is worth noticing that for certain measurement temperatures hollow and solid symbols can be found.

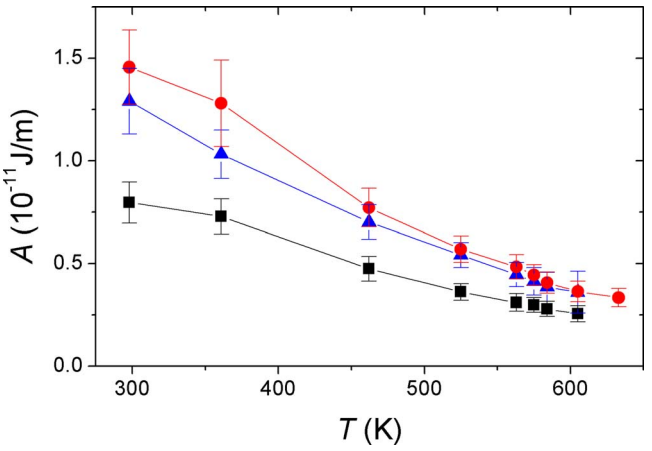

FIG. 11. (Color online) Calculated exchange stiffness constant as a function of temperature.

of transformation. Therefore, a linear behavior of $(\mu_0 M_S H_C)^2$ versus X_{DSC}^4 is expected with a value at $X_{\mathrm{DSC}}=0$ equal to $(p_C\langle K_U\rangle)^2$ and a slope:

$$m = p_C^2 f^4 \frac{K_1^8 \langle D\rangle^{12}}{A^6}. \tag{9}$$

Figure 10 shows, as an example, this plot for Zr alloy using data obtained at different temperatures. For each measurement temperature, T_m, the expected linear behavior is fulfilled (regression factor $r>0.9$) when T_m is below the Curie temperature of the amorphous phase of samples, T_C^{am}, with $X_{\mathrm{DSC}}<0.9$. It is worth noting that linearity is not lost when T_m is above T_C^{am} for $X_{\mathrm{DSC}}=0.9$.

A qualitative explanation could be given after the model developed by Hernando *et al.*,[15] where A is substituted by γA, being

$$\gamma = e^{-\Lambda/L_{\mathrm{am}}} \tag{10}$$

being

$$\Lambda = \langle D\rangle \left(\frac{1}{X_C}\right)^{1/3} - \langle D\rangle, \tag{11}$$

where L_{am} is the exchange correlation length of the amorphous matrix and γ is a parameter (from 0 to 1) that describes the ability of the amorphous matrix for transmitting the exchange interaction between nanocrystals. For low values of D/L_{am}, γ is independent of crystalline fraction,[15] which supports the linear fitting observed for low temperatures in Fig. 10. Increasing the temperature, L_{am} decreases and its dependence on the crystalline fraction can no longer be neglected as the D/L_{am} ratio increases (see Fig. 1 in Ref. 15), explaining the deviation from the linearity of the high temperature data of Fig. 10 for low crystalline fractions. Values of Λ could also be very small for large values of crystalline volume fraction and small crystal size as those reported here (5 nm), leading to $\gamma\sim 1$. In fact, single phase model developed by Herzer only fails for low crystalline fractions close to the Curie temperature of the amorphous phase, where a maximum in coercivity is only explained by two phase models. At large crystalline volume fractions ($X_{\mathrm{DSC}}\geq 0.6$ in the present paper), this maximum is not detected and the effect of the amorphous phase could be neglected considering that the nanocrystals are so close to each other that the exchange interaction is possible.

The slopes described by expression (9) were obtained for different temperatures and taking into account the linear temperature dependence of $K_1=aT+b$, [K_1 decreases from 46 to 13 kJ/m^3 increasing T from 273 to 673 K (Ref. 35)], values of the exchange stiffness constant can be obtained as a function of the temperature from

$$A(T) = p_C^{1/3} f^{2/3} \frac{(aT+b)^{4/3}\langle D\rangle^2}{m(T)^{1/6}}, \tag{12}$$

Figure 11 shows A as a function of the temperature, neglecting the effect of f and p_C, as $(f^2 p_C)^{1/3}\sim 1$. The obtained values are almost composition independent, in agreement with the expected similar composition of the crystalline phase formed in all the studied alloys and are of the order of that of pure Fe ($A=1.74\times 10^{-11}$ J m^{-1}) (Ref. 28) and those of amorphous alloys.[15] It is worth mentioning that these results were obtained without any free parameter but just using the experimentally measured values of coercivity, saturation magnetization, volume fraction, and crystal size obtained in this study and the thermal dependence of K_1.[35] The observed continuous decrease in A as temperature increases could also be qualitatively explained by the two phase model developed by Hernando *et al.*:[15] for a given value of X_C and D, γ decreases continuously from 1 to 0 approaching the Curie temperature of the amorphous phase but its dependence on the crystalline fraction is out of consideration in this study, where results are obtained as an average from samples with different X_{DSC}. However, for $\langle D\rangle=5$ nm and $L_{\mathrm{am}}\sim 30$ nm, γ changes $\sim 15\%$ from $X_C=0.1$ to 0.9.[15]

The values of $\langle K_U\rangle$ exhibit large error bars but following the assumptions done on the independence of this parameter

on X_{DSC}, $p_C\langle K_U\rangle \sim 2$ kJ m^{-3} can be estimated without distinguishable difference between the three studied compositions.

V. CONCLUSIONS

The temperature dependence of magnetic properties has been studied for nanocrystalline $Fe_{60}Co_{18}Cu_1B_{15}Nb_{6-x}Zr_x$ ($x=0$, 3, 6) samples at different stages of devitrification. The size of the formed nanocrystals (~ 5 nm) is almost constant with nanocrystallization progress, supporting the instantaneous growth approximation to describe the kinetics of the transformation.

A good correlation could be found between the different parameters related with the transformed fraction: X_{DSC}, A_{cryst}, $\langle HF\rangle$, and σ_S. Soft magnetic properties at room temperature are enhanced for low crystalline fraction samples, but deteriorate for samples with a high crystalline fraction. However, the thermal dependence of magnetic properties is reduced as nanocrystallization progresses, which is a positive factor for technical applications in a broad temperature range.

The Curie temperature of the residual amorphous phase decreases as nanocrystallization progresses, being higher for 6 at. % Zr alloy than for Nb containing alloys for a constant value of X_{DSC}.

The thermal dependence of the magnetic anisotropy can be interpreted in the framework of the extended two phase model of random anisotropy applied to nanocrystalline systems. Results yield the thermal dependence of the exchange stiffness constant with changing composition and microstructure without using any free parameter.

ACKNOWLEDGMENTS

This work was supported by the Ministry of Science and Innovation (MICINN) and EU FEDER (Project Nos. MAT2007-65227 and CIT420000-2008-9), the PAI of the Regional Government of Andalucía (Project No. P06-FQM-01823), the Hispano-Hungarian bilateral cooperation Project (No. 2006HU0015) and the Hungarian Scientific Research Fund (Grant No. OTKA 68612). J.S.B. acknowledges a research contract from Junta de Andalucía.

[1] M. E. McHenry, M. A. Willard, and D. E. Laughlin, Prog. Mater. Sci. **44**, 291 (1999).
[2] Y. Yoshizawa, S. Oguma, and K. Yamaguchi, J. Appl. Phys. **64**, 6044 (1988).
[3] K. Suzuki, A. Makino, N. Kataoka, A. Inoue, and T. Matsumoto, Mater. Trans., JIM **32**, 93 (1991).
[4] M. A. Willard, D. E. Laughlin, M. E. McHenry, D. Thoma, K. Sickafus, J. O. Cross, and V. G. Harris, J. Appl. Phys. **84**, 6773 (1998).
[5] M. A. Willard, M. Q. Huang, D. E. Laughlin, M. E. McHenry, J. O. Cross, and V. G. Harris, J. Appl. Phys. **85**, 4421 (1999).
[6] X. Liang, T. Kulik, J. Ferenc, and B. Xu, J. Magn. Magn. Mater. **308**, 227 (2007).
[7] I. Skorvanek, J. Marcin, T. Krenicky, J. Kovac, P. Svec, and D. Janickovic, J. Magn. Magn. Mater. **304**, 203 (2006).
[8] Zs. Gercsi, F. Mazaleyrat, and L. K. Varga, J. Magn. Magn. Mater. **302**, 454 (2006).
[9] M. Kowalczyk, J. Ferenc, X. B. Liang, and T. Kulik, J. Magn. Magn. Mater. **304**, e651 (2006).
[10] J. S. Blázquez, C. F. Conde, V. Franco, A. Conde, and L. F. Kiss, J. Appl. Phys. **103**, 07E721 (2008).
[11] D. H. Ping, Y. Q. Wu, K. Hono, M. A. Willard, M. E. McHenry, and D. E. Laughlin, Scr. Mater. **45**, 781 (2001).
[12] Y. Zhang, J. S. Blázquez, A. Conde, P. J. Warren, and A. Cerezo, Mater. Sci. Eng., A **353**, 158 (2003).
[13] J. S. Blázquez, V. Franco, and A. Conde, J. Phys. Condens. Matter **14**, 11717 (2002).
[14] G. Herzer, IEEE Trans. Magn. **25**, 3327 (1989).
[15] A. Hernando, M. Vázquez, T. Kulik, and C. Prados, Phys. Rev. B **51**, 3581 (1995).
[16] K. Suzuki and J. M. Cadogan, Phys. Rev. B **58**, 2730 (1998).
[17] T. Kulik, A. Wlazlowska, J. Ferenc, and J. Latuch, IEEE Trans. Magn. **38**, 3075 (2002).
[18] M. Daniil, M.A. Willard, J. Appl. Phys. **103**, 07E727 (2008).
[19] G. Herzer, Scr. Metall. Mater. **33**, 1741 (1995).
[20] R. C. O'Handley, *Modern Magnetic Materials: Principles and Applications* (Wiley, New York, 1999).
[21] J. S. Blázquez, C. F. Conde, A. Conde, S. Roth, and A. Güth, J. Magn. Magn. Mater. **304**, e627 (2006).
[22] R. A. Brand, J. Lauer, and D. M. Herlach, J. Phys. F: Met. Phys. **13**, 675 (1983).
[23] J. S. Blázquez, M. Millán, C. F. Conde, and A. Conde, Philos. Mag. **87**, 4151 (2007).
[24] J. S. Blázquez, V. Franco, M. Millán, C. F. Conde, and A. Conde, J. Non-Cryst. Solids **354**, 3597 (2008).
[25] J. S. Blázquez, V. Franco, and A. Conde, J. Alloys Compd. **422**, 32 (2006).
[26] V. Franco, C. F. Conde, A. Conde, and L. F. Kiss, Phys. Rev. B **72**, 174424 (2005).
[27] J. S. Blázquez, V. Franco, C. F. Conde, and A. Conde, J. Magn. Magn. Mater. **254–255**, 460 (2003).
[28] B. D. Cullity, *Introduction to Magnetic Materials* (Addison-Wesley, Reading, 1972), pp. 291 and 617.
[29] V. Franco, C. F. Conde, A. Conde, B. Varga, and A. Lovas, J. Magn. Magn. Mater. **215–216**, 404 (2000).
[30] L. F. Kiss, D. Kaptás, J. Balogh, J. Gubicza, T. Kemény, and I. Vincze, J. Magn. Magn. Mater. **272–276**, 1410 (2004).
[31] C. F. Conde, J. S. Blázquez, V. Franco, A. Conde, P. Svec, and D. Janickovic, Acta Mater. **55**, 5675 (2007).
[32] V. Franco, J. S. Blázquez, C. F. Conde, and A. Conde, Appl. Phys. Lett. **88**, 042505 (2006).
[33] H. P. J. Wijn, *Landolt-Börnstein: Magnetische Eigenschaften von Metallen* (Springer-Verlag, Berlin, 1991), Vol. 19, pp. 93, 103, and 106.
[34] J. S. Blázquez, V. Franco, A. Conde, M. R. J. Gibbs, H. A. Davies, and Z. C. Wang, J. Magn. Magn. Mater. **250**, 260 (2002).
[35] R. M. Bozorth, J. Appl. Phys. **8**, 575 (1937).